symmetry

MDPI

*Review*

# Continuous-Flow Photocatalytic Microfluidic-Reactor for the Treatment of Aqueous Contaminants, Simplicity, and Complexity: A Mini-Review

**Zhongwei Gao [1], Changqing Pan [1], Chang-Ho Choi [2] and Chih-Hung Chang [1,*]**

[1] School of Chemical, Biological, and Environmental Engineering, Oregon State University, Corvallis, OR 97331, USA; gaoz@oregonstate.edu (Z.G.); panc@oregonstate.edu (C.P.)
[2] Department of Chemical Engineering, Gyeongsang National University, 501 Jinju-daero, Jinju-si 52828, Korea; ch_choi@gnu.ac.kr
* Correspondence: Chih-Huang.Chang@oregonstate.edu; Tel.: +1-541-737-8548; Fax: +1-541-737-4600

**Abstract:** Water pollution is a growing global issue; there are many approaches to treating wastewater, including chemical coagulation, physical adsorption, and chemical oxidation. The photocatalysis process has provided a solution for removing pollutants from wastewater, where the pair of the photoelectron and hole works through an asymmetric way to degrade the contaminants under UV irradiation. This method offers an alternative route for treating the pollutant with a lower energy cost, high efficiency, and fewer byproducts. A continuous-flow microfluidic reactor has a channel size from tens to thousands of micrometers, providing uniform irradiation and short diffusion length. It can enhance the conversion efficiency of photocatalysis due to the simple spatial symmetry inside the microreactor channel and among the individual channels. In addition, the bandgap of $TiO_2$, ZnO, or other photocatalyst nanoparticles with symmetric crystal structure can be modified through doping or embedding. In this mini-review, a review of the reported continuous-flow photocatalytic microfluidic reactor is discussed from the perspective of both microreactor design and material engineering.

**Keywords:** microfluidic reactor; photocatalysis; microreactor design; water treatment

check for updates

**Citation:** Gao, Z.; Pan, C.; Choi, C.-H.; Chang, C.-H. Continuous-Flow Photocatalytic Microfluidic-Reactor for the Treatment of Aqueous Contaminants, Simplicity, and Complexity: A Mini-Review. *Symmetry* **2021**, *13*, 1325. https://doi.org/10.3390/sym13081325

Academic Editors: Wladimir Reschetilowski and Ekaterina Borovinskaya

Received: 1 April 2021
Accepted: 5 July 2021
Published: 23 July 2021

**Publisher's Note:** MDPI stays neutral with regard to jurisdictional claims in published maps and institutional affiliations.

**Copyright:** © 2021 by the authors. Licensee MDPI, Basel, Switzerland. This article is an open access article distributed under the terms and conditions of the Creative Commons Attribution (CC BY) license (https://creativecommons.org/licenses/by/4.0/).

## 1. Introduction

Water is an essential natural resource for the whole of earth's ecosystem, covering more than 70% of the earth's surface. High-level pollutants in wastewater from in-creased human activities must be separated or made harmless before discharge into streams or before reuse. Heavy metals such as lead (Pb), mercury (Hg), cadmium (Cd), copper (Cu), and arsenic (As) can cause severe health damage to both aquatic organisms and humans. Many toxic herbicides and pesticides that are listed as known carcinogens are released to the soil and water bodies during agriculture activities. Organic pollutants from paper, textile, or other industries have long been of concern due to their long-term persistence in the natural water system, leading to critical environmental hazards. For example, harmful and toxic organic dyes and their metabolites have been posing severe threats to humans due to their effects on the liver, kidney and cardiovascular system [1]. Mercury can accumulate in fish, and mercury-contaminated fish can cause neurological dysfunction in humans [2]. Japan decided to release nuclear wastewater into the Pacific Ocean from the Fukushima Daichi Nuclear Power Plant on 13 April 2021, which can cause a long-term impact on the environment [3]. Pathogenic bacteria in the contaminated water can also cause various diseases, such as diarrhea and gastrointestinal illness [4]. Many existing approaches can treat the wastewater to reduce the contamination. For example, methods have been developed to remove the dyes in water, including chemical coagulation, physical adsorption, and chemical oxidation using ozone or $H_2O_2$ [5]. However, the coagulated or adsorbed dyes are only transferred from one phase to another and can still act as a pollution

source. In contrast, chemical oxidation involves toxic oxidants and consumes excessive energy. The photocatalysis process provides an alternative solution to remove the contaminants in the wastewater with benefits of a lower energy cost, high efficiency in destroying the organic dyes, and less byproduct waste. Studies have shown that photocatalysis can be adopted to eliminate all types of water contamination, including the degradation of organic dyes [6–8], removal of metals [2,9,10], degradation of antibiotics [11–13], removal of radioactive materials [14–16], and the inactivation of bacteria [17,18]. In some typical photocatalytic wastewater treatments, the organic dyes are eliminated by employing semiconductor materials such as $TiO_2$ and ZnO under UV irradiation [19]. In particular, as a compound semiconductor with a direct bandgap of 3.37 eV, ZnO has been widely studied due to its good photocatalytic performance and ease of synthesis [20–22]. The conventional suspension-based photocatalytic reactor is not efficient from the reactor design perspective because photocatalytic colloidal nanoparticles readily aggregate in the suspension system. The light intensity varies upon the location of the reactor. The photocatalyst has been integrated into a microreactor system to address these issues. The microfluidic-based photocatalytic reactor, with some inherent advantages of the microreactor system, such as the high surface-to-volume ratio, short diffusion distances, and rapid mass transfer, has improved the photocatalytic performance degrading organic contaminants [23,24].

There are three main objectives for this review paper: (1) providing insights into some basic working principles of microfluidic-based photocatalysis, (2) highlighting innovation in photocatalytic microreactor design, fabrication, and catalyst material engineering; and (3) identifying future directions. Understanding reactor and catalyst design principles can help researchers develop more efficient microfluidic-based photocatalytic reactors to treat aqueous contaminants.

## 2. Mechanism of the Photocatalysis

### *2.1. Redox-Based Heterogeneous Photocatalysis*

Most microfluidics and suspension systems that degrade organic compounds are based on the same mechanism. In a typical photocatalysis process (Figure 1), as the photocatalytic materials absorb the light with sufficient energy, electrons in the valence band are excited to the conduction band while leaving holes in the valence band. ZnO is used as a typical photocatalyst example (Equation (1)) [25]. These electrons in the conduction band ($e^-_{CB}$) and holes in the valence band ($h^+_{VB}$) either undergo recombination and release heat (Equation (2)) or react with water and dissolved oxygen ($O_2$) in the aqueous medium. The holes in the valence band can react with the water to produce the hydroxyl radicals (Equation (3)). The holes in the valence band can also directly convert the organic pollutant to intermediate compounds, which are highly reactive and thus lead to the subsequent oxidation process (Equation (4)). In the conduction band, the electrons can react with $O_2$ molecules to form superoxide radicals (Equation (5)) and further form the hydroperoxyl radicals (Equation (6)). All these resultant radicals are strong oxidants that play a crucial role in degrading organic pollutants, followed by subsequent mineralization at the end (Equations (7) and (8)).

$$ZnO \xrightarrow{h\nu} ZnO\left(e^-_{CB} + h^+_{VB}\right) \quad (1)$$

$$e^-_{CB} + h^+_{VB} \rightarrow heat \quad (2)$$

$$h^+_{VB} + H_2O \rightarrow \bullet OH + H^+ \quad (3)$$

$$h^+_{VB} + \text{organic pollutant} \rightarrow \text{degraded products} \quad (4)$$

$$e^-_{CB} + O_2 \rightarrow \bullet OO^- \quad (5)$$

$$\bullet OO^- + H^+ \rightarrow \bullet OOH \quad (6)$$

$$\bullet OH + \text{organic pollutant} \rightarrow \text{degraded products} \quad (7)$$

$$\bullet OOH + \text{organic pollutant} \rightarrow \text{degraded products} \quad (8)$$

The following reaction is an example of the degradation of formaldehyde (HCHO), a common organic small-molecule pollutant:

$$HCHO + \bullet OH \rightarrow HCO\bullet + H_2O \quad (9)$$

$$HCO\bullet + \bullet OH \rightarrow HCOOH \quad (10)$$

$$HCOOH + 2h^+_{VB} \rightarrow CO_2 + 2H^+ \quad (11)$$

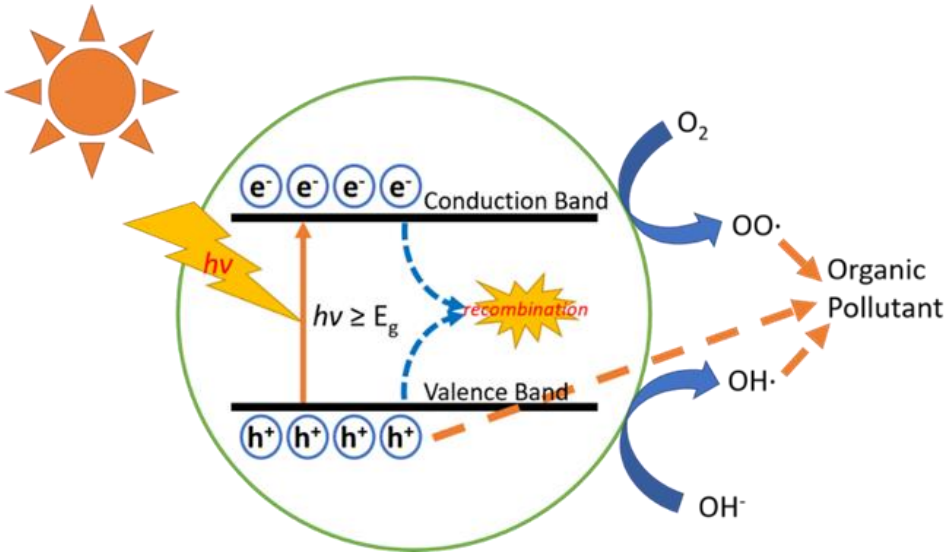


**Figure 1.** Schematic illustration of the photocatalysis process.

*2.2. Photo-Assisted Fenton Reaction*

The Fenton reaction is a homogenous oxidation process, which H. J. Fenton first described [26]. Iron (II) ($Fe^{2+}$) is used as a catalyst to enhance the oxidative potential of $H_2O_2$. The original Fenton process can be described as the following reactions [27]:

$$Fe^{2+} + H_2O_2 \rightarrow Fe^{3+} + \bullet OH + OH^- \quad (12)$$

$$\bullet OH + H_2O_2 \rightarrow \bullet OOH + H_2O \quad (13)$$

$$Fe^{2+} + \bullet OH \rightarrow Fe^{3+} + OH^- \quad (14)$$

$$Fe^{3+} + \bullet OOH \rightarrow Fe^{2+} + O_2 + H^+ \quad (15)$$

$$\bullet OH + \bullet OH \rightarrow H_2O_2 \quad (16)$$

$$\bullet OH + \text{organic pollutant} \rightarrow \text{degraded products} \quad (17)$$

The $Fe^{3+}$ to $Fe^{2+}$ reaction (Equation (15)) is slow, and once all $Fe^{2+}$ ions are oxidated to $Fe^{3+}$, the reaction does not proceed. UV irradiation can regenerate the $Fe^{2+}$ by photo-reduction of $Fe^{3+}$ (Equations (18) and (19)). Meanwhile, $H_2O_2$ also photolyzes with UV light and generates more radicals for pollution degradation (Equation (20)).

$$Fe^{3+} + H_2O + h\nu \rightarrow Fe^{2+} + \bullet OH + H^+ \quad (18)$$

$$Fe^{3+} + H_2O_2 + h\nu \rightarrow Fe^{2+} + \bullet OOH + H^+ \quad (19)$$

$$H_2O_2 + h\nu \rightarrow 2\ \bullet OH \quad (20)$$

### *2.3. Microbe-Photocatalyst Hybrids*

A microbe-photocatalyst hybrids (MPH) system is a combination of microbial cells with photocatalyst coating on the surface. The photoelectron generated from the photocatalyst can be transported to the microorganism for enzyme-catalyzed reactions [28], meanwhile the hole can still degrade the organic pollutant in the water.

Microbial sedimentation has been used to settle the dissolved heavy metal ions [29]. The deposited nanomaterials on the microorganisms' surfaces can work as the photocatalyst and form the MPH system with microorganisms. Zuo et al. proposed a comprehensive strategy for heavy metal treatment by MPH: using dissolved heavy metal ions to synthesize the photocatalyst, reducing the heavy metal ions that are toxic in high valence states such as $Cr^{6+}$ and $Se^{4+}$, and using heavy metal ions that are toxic in low valence states as the sacrificial electron donors [30].

## 3. Kinetics of Microfluidics Photocatalysis

### *3.1. Comparison of Microfluidics with a Suspension System in Photocatalytic Activity*

In conventional wastewater treatment, light illuminates the suspension composed of photocatalyst nanoparticles (NPs) and pollutants under vigorous stirring, as shown in Figure 2a [31]. This suspension-based system inherently imposes a large gradient in temperature, acidity, and concentration over spatial position and reaction time. Additionally, the photocatalyst NPs should be removed after the reaction, which is a formidable process and requires excessive energy and time.

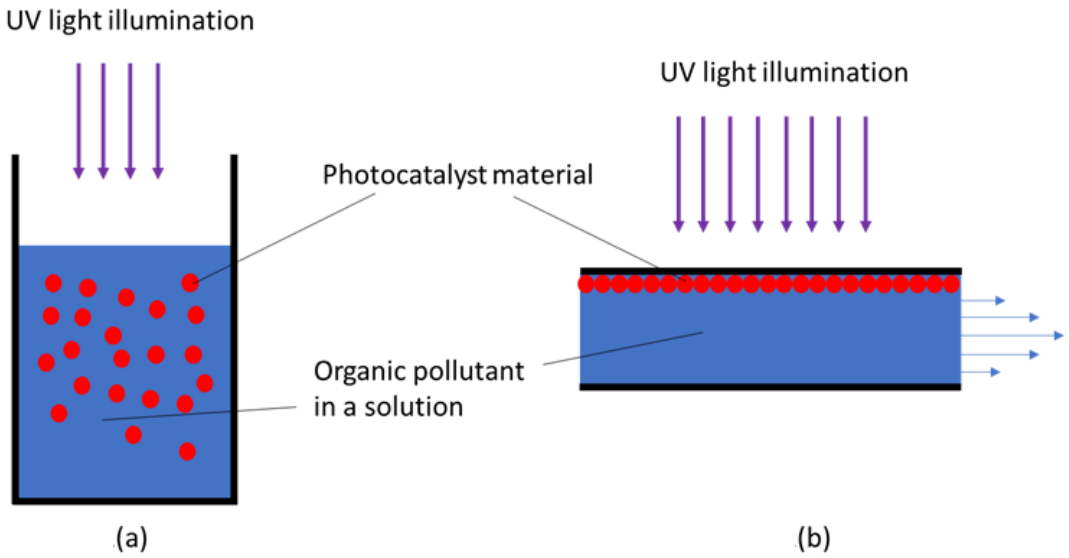


**Figure 2.** Schematic illustrations of (**a**) suspended photocatalysis and (**b**) microfluidic reactor immobilized with a photocatalyst.

Immobilized photocatalytic materials on the internal surface of the microreactor can overcome these problems, and the organic pollutant solution is subject to flow inside the microreactor [32]. A microfluidic reactor, with a channel size within the sub-millimeter level, can provide uniform irradiation of light and short diffusion length for highly efficient photocatalytic performances [33]. As shown in a typical microfluidic-based photocatalysis process in Figure 2b, a solution stream containing the target organic compounds flows through the microchannel, where the photocatalyst is immobilized on the surface of the channel. When UV light illuminates the whole channel, a strong oxidant such as a hydroxyl radical generated by the photocatalyst reacts with organic dyes to decompose them [34–36]. Compared with the suspension system, the microfluidic-based process has several advantages that can enhance the photocatalytic performance: (1) The pollutants can contact the photocatalytic materials more efficiently due to the short diffusion distance. (2) The surface area of the photocatalytic materials can be increased by reasonably designing the microre-

actor geometry. (3) The degradation of the organic pollutants can be kinetically tailored by the flow rate of the solution and reactor dimension, which eventually leads to the optimal process conditions to degrade the organic pollutants best. (4) Lastly, a remarkable feature of the microfluidic-based system is the reuse of photocatalytic materials without an additional recovery process.

### *3.2. Photocatalytic Reaction Kinetic Study of Organic Compound Degradation in a Microfluidic System*

To evaluate the performance of the photocatalyst, one direct method is to use the percentage of degradation [37]:

$$\text{degradation } \% = \left(1 - \frac{C_t}{C_0}\right) \times 100\% \tag{21}$$

where $C_t$ is the measured concentration of the pollutant after degradation for a certain time $t$, $C_0$ is the original concentration of the pollutants before the degradation. A higher degradation percentage means less pollutants remain, and the efficiency of the device is higher.

Many factors can influence the performance of the photocatalyst, including the temperature, light source, pollutant concentration, and for the photocatalytic process in a microfluidic reactor, the operation condition also plays an important role, such as the flow rate of the device, the area of the photocatalyst, and the cycle of the flow.

Herein, some of the results from the literature are presented to give a general idea of the efficiency of a photocatalytic microfluidic reactor. Meng et al. studied photocatalytic microreactor efficiency using nanofibrous $TiO_2$, and found that the degradation percentage of the nanofibrous $TiO_2$ was about 20% at the first cycle, and increased to about 60% after 10 cycles [38]. Roselin et al. used ZnO for photocatalytic degradation of Reactive Red 22 in a flow reactor, and the degradation percentage reached about 98.3% in 6 cycles [39]. In Moussavi's study, the reduction percentage of Cr(VI) can reach 100% in less than 10 min [40].

In a microfluidic reactor, the flow rate can influence the degradation of the pollutants. To exclude the transport effect of the reactor, a kinetic study is performed to better understand the performance of a photocatalytic device.

In a microfluidic-based photocatalytic process, the organic pollutant compound molecules' transport to the photocatalytic materials and their subsequent adsorption on these photocatalytic materials play an essential role in determining the degradation rate of the organic molecules. Some computational and empirical studies have been carried out to elucidate the reaction kinetics of the degradation in this context.

Behnajady et al. experimentally studied the photocatalytic degradation of an azo dye (AR27) in a continuous flow photoreactor. Based on the experimental results, they suggested a kinetic degradation model by using the Langmuir–Hinshelwood mechanism [37]. The kinetics of photocatalysis in a suspension system follows a pseudo-first-order reaction Equation (22).

$$r = -\frac{dC}{dt} = k_{\text{obs}} C \tag{22}$$

where $r$, $k_{\text{obs}}$, and $C$ are the reaction rate, observed rate constant, and the organic compound's concentration, respectively. Note that the observed rate constant is a function of competitive adsorption of intermediates on the photocatalyst surface.

The microfluidic device, modeled as a plug flow reactor, assumes a homogenous fluid mixing in the radial and angular direction. The mass balance equation of the plug flow reactor at the steady-state can be expressed as follows:

$$\frac{dC}{dV_D} = \frac{r}{Q} \tag{23}$$

where $Q$ and $V_D$ are the flow rate of the solution and the reactor's volume, respectively. Substituting Equation (22) into Equation (23) gives:

$$\frac{dC}{dV_D} = \frac{k_{obs}C}{Q} \tag{24}$$

Solving Equation (24) obtains:

$$\ln \frac{C_{outlet}}{C_{inlet}} = -\frac{V_D k_{obs}}{Q} = -\frac{Sk_{obs}}{Q}l = -k'_{obs}l \tag{25}$$

$$k'_{obs} = \frac{Sk_{obs}}{Q} \tag{26}$$

$C_{outlet}$ and $C_{inlet}$ are the concentration of azo dye leaving and entering the microfluidic device, respectively; $S$ is the reactor's cross-section area, and $l$ is the channel length and $k'_{obs}$ is the observed reaction rate constant as a function of channel length and flow rate.

The photodegradation rate was estimated under different channel flow rates and lengths by applying the kinetics study. The results indicate that with the decrease of the flow rate, the degradation rate increased. The linear relation indicates the pseudo-first-order reaction kinetics, as shown in Figure 3.

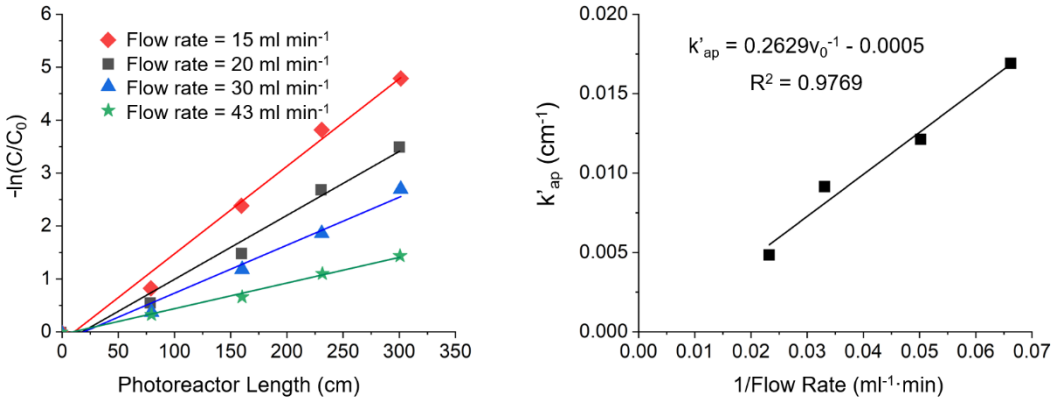


**Figure 3.** (**a**) Linear regression of photocatalytic degradation of AR27 in the continuous-flow photoreactor in UV/$TiO_2$ process and (**b**) relation between flow rate and reaction rate constant [37].

Corbel et al. studied the mass transfer rate and relevant modeling in a microchannel photocatalytic reactor [41]. Degradation of salicylic acid (S.A.) was conducted in two microreactors with different depths. The experimental results in Figure 4a show that the conversion yield of S.A. in the microreactor with a depth of 0.5 mm (R1) is higher than the reactor with a depth of 0.75 mm (R2) due to the lower limitation by mass transfer in reactor R1. To further study the kinetics of degradation, two kinetics models were studied: a kinetics model (sim. L.H.), which is based on the Langmuir–Hinshelwood kinetic equation, suggests the removal rate of S.A. is governed by the balance between the flux of S.A. to the photocatalytic materials and the photodegradation reaction. On the other hand, the different models (sim. transf.) only consider mass transport from the bulk to the photocatalytic materials. The comparison results of the two models are shown in Figure 4b, indicating that the mass transport model agrees with the experiments. With the mass transport model and conversion yield data, the external mass transfer constant was also estimated.

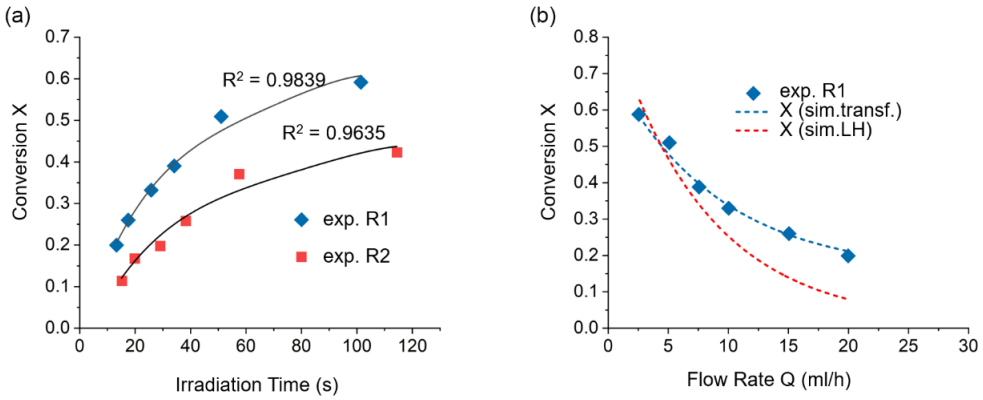


**Figure 4.** (**a**) Experimental photocatalytic conversion yield of S.A. in R1 and R2 as a function of the irradiation time and (**b**) comparison of the two models with experimental data for R1 [41].

### *3.3. Comparison between the Batch Reactor and Microfluidic Reactor*

A comparison has been made between the macroscopic reactor and the microfluidic reactor. Mendoza et al. studied the transition from conventional batch to microfluidic process for the photooxygenation of methionine and enhanced the initial rate of photooxygenation and space-time yield using a continuous flow reactor [42]. In addition, their study also showed that both mass transfer limitations and light penetration play essential roles in the process.

Zhan et al. provided a study on the kinetics model of immobilized photocatalyst in batch reactor and microfluidic reactor to compare the kinetics between batch reactor and continuous flow reactor [43]. The Langmuir–Hinshelwood (LH) mechanism was used to describe the heterogeneous photocatalytic reactions, and the intrinsic reaction rate can be expressed as:

$$r_{\text{int}} = \frac{k_{\text{int}} m_{\text{cat}} K_{\text{LH}} C}{1 + K_{\text{LH}} C} \tag{27}$$

where $m_{\text{cat}}$ is the catalyst mass, $K_{\text{LH}}$ is the adsorption equilibrium constant of the reactant, $C$ is the mass concentration of the pollutant in the liquid phase, and $k_{\text{int}}$ is the intrinsic reaction rate constant.

In a bath reactor, the observed pollutants consumption rate can be expressed as:

$$R_{\text{obs}} = V_{\text{batch}} \frac{dC_{\text{b}}}{dt} \tag{28}$$

where $V_{\text{batch}}$ is the volume of the batch reactor, and $\frac{dC_{\text{b}}}{dt}$ is the observed change of the pollutant concentration in the bulk solution with time. In a bath reactor, the liquid concentration $C$ is equal to the pollutant concentration in the bulk $C_{\text{b}}$, the change of the pollutant concentration can be expressed as:

$$\frac{dC_{\text{b}}}{dt} = -\frac{1}{V_{\text{batch}}} k_{\text{int}} \frac{m_{\text{cat}} K_{LH} C_{\text{b}}}{1 + K_{LH} C_{\text{b}}} \tag{29}$$

On the other hand, in a microfluidic reactor, the observed pollutants consumption rate can be expressed as:

$$\frac{dC_{\text{b}}}{dz} = \frac{1}{\dot{V} L_{\text{MR}}} R_{\text{obs}} \tag{30}$$

where $\dot{V}$ is the flow rate of the solution in the microreactor, and $L_{\text{MR}}$ is the length of the microreactor. Due to the convection of the solution, the concentration of the pollutant in the bulk solution $C_{\text{b}}$ is different from the photocatalyst surface $C_{\text{S}}$. A mass balance between

the diffusive flux to the catalyst surface and the rate of consumption on the catalyst surface is established to solve the Equations (27) and (30):

$$\beta_m(C_b - C_S) = \frac{1}{A_{cat}} k_{int} \frac{m_{cat} K_{LH} C_S}{1 + K_{LH} C_S} \quad (31)$$

where the $\beta_m$ is the mass transfer coefficient, and $A_{cat}$ is the external surface area of the catalyst layer.

## 4. Design and Fabrication of the Microfluidic Reactor

### *4.1. Geometric Design of the Microfluidic Photocatalysis Reactor*

Various design concepts have been introduced to fabricate the microfluidic photocatalytic device to enhance the target compounds' conversion. Microreactors with different geometries have been reported to increase efficiency and study the kinetics of photocatalysis under continuous flow conditions. One convenient approach is to load a micro-capillary tube with photocatalysts on its inner walls, as illustrated in Figure 5a. The degradation of the target pollutant occurs on the inner walls' surface when the solution flows through the microchannels [24]. Another way is to fabricate the photocatalyst on a glass substrate, and the solution containing the pollutant flows through the surface guided by a channel. The simplest one is a line channel, as illustrated in Figure 5b [44]. Polyline channels [45] and parallel line channels [46] have also been employed to use more surface area of the substrate, as shown in Figure 5c,d. These approaches increase the contacting area between the solution and photocatalytic surface; thus, enhancing the photocatalytic conversion can be expected. A planar channel with pillar arrays on the substrate was fabricated to increase the contacting area further, as illustrated in Figure 5e [47]. Figure 5f shows that it is possible to increase the surface area of the loaded catalyst by introducing a side lobe structure on the channel [48].

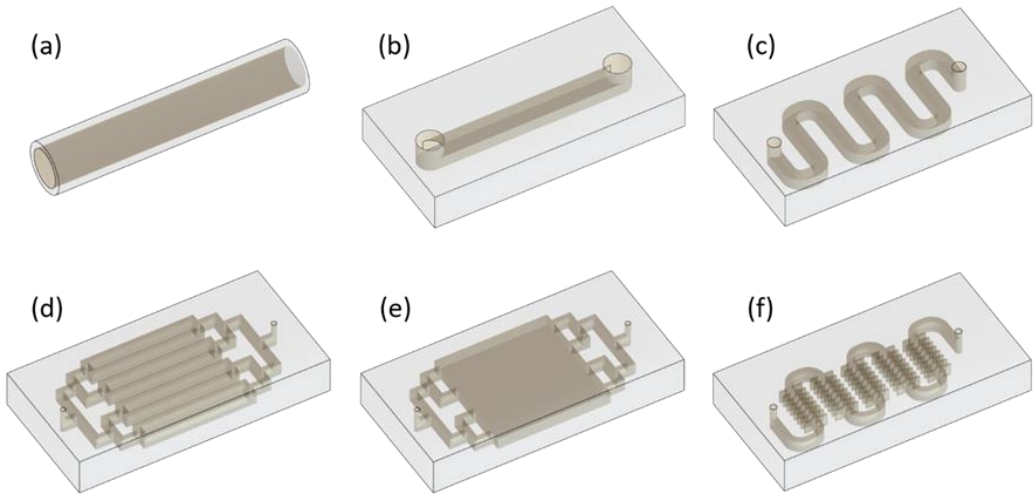


**Figure 5.** Typical microfluidic photocatalysis reactors with symmetric designs. (**a**) Capillary microchannel, (**b**) straight line microchannel, (**c**) polyline microchannel, (**d**) parallel line microchannel, (**e**) planar channel, and (**f**) line channels with side lobes.

Visan et al. developed a single-channel microreactor embedding the immobilized photocatalytic materials to study the intrinsic degradation kinetics of cortisone 21-acetate (C.A.) [45]. The reactor performance was evaluated, using a single channel microreactor, shown in Figure 6a, by first-order reaction rate with either light independence or light dependency described by a photon-absorption carrier generation mechanism. This modeling can lead to a rational reactor design and easy optimization. Castedo et al. fabricated multiple parallel channels for the photocatalytic generation of hydrogen simply and efficiently using 3D printing and PDMS polymerization, shown in Figure 6b [46]. The Au/$TiO_2$

photocatalyst was immobilized on the silicon microchannel wall, and the performance of the microreactor was tested under different water-ethanol gaseous mixtures. Han et al. designed a planar chamber with a large area and high-density ZnO nanowires to achieve high photocatalytic efficiency for degradation of methylene blue, shown in Figure 6c [49].

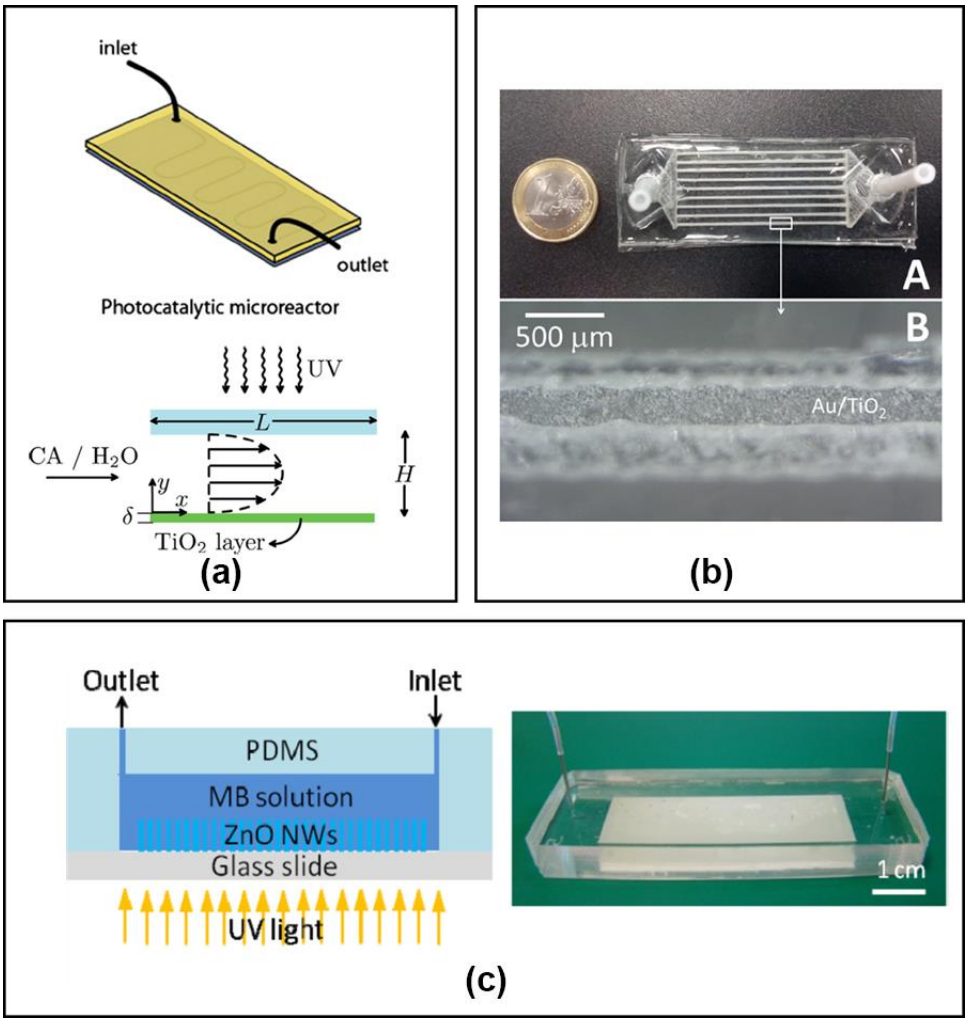


**Figure 6.** (**a**) Single channel design and the study of the kinetics [45], (**b**) optical image of parallel multiple channels coated with photocatalyst [46], and (**c**) the planar channel design [49].

### *4.2. The Light Source for the Photocatalysis*

The majority of the reports used $TiO_2$ and ZnO as a photocatalyst. As a result of the bandgap values of $TiO_2$ and ZnO, a UV light source is commonly used to enable the electrons to move from the valence band to the conduction band. A doped $TiO_2$ or ZnO can lower the bandgap value, which allows photocatalysis under visible light. Another approach introduces a lower bandgap material and creates a heterojunction with $TiO_2$ or ZnO to broaden the light spectrum's utilization. Wang et al. described a microfluidic reactor that uses a $BiVO_4/TiO_2$ heterojunction photocatalyst [50]. $BiVO_4$ can absorb visible light, and $TiO_2$ can absorb near UV light. They used a Xe lamp as a light source to simulate sunlight. Using $BiVO_4$ on indium tin oxide (ITO) coated glass, the same group also described microfluidic photo-electrocatalytic reactors with an integrated visible-light source [51].

In a typical microfluidic photocatalytic device, the light source is placed outside the reactor. Inevitably, part of the incident light can be reflected and absorbed by the window of a microreactor, resulting in a loss of photons and energy waste. Some studies have sought out to mitigate this issue. For example, a light source was inserted into a tubular

reactor so that the light can directly shine on the solution and the photocatalyst [52]. A rotating disk or tube photocatalytic reactor, shown in Figure 7, can be used where a thin liquid film carried by a rotating disk or tube is directly exposed to the UV light [53].

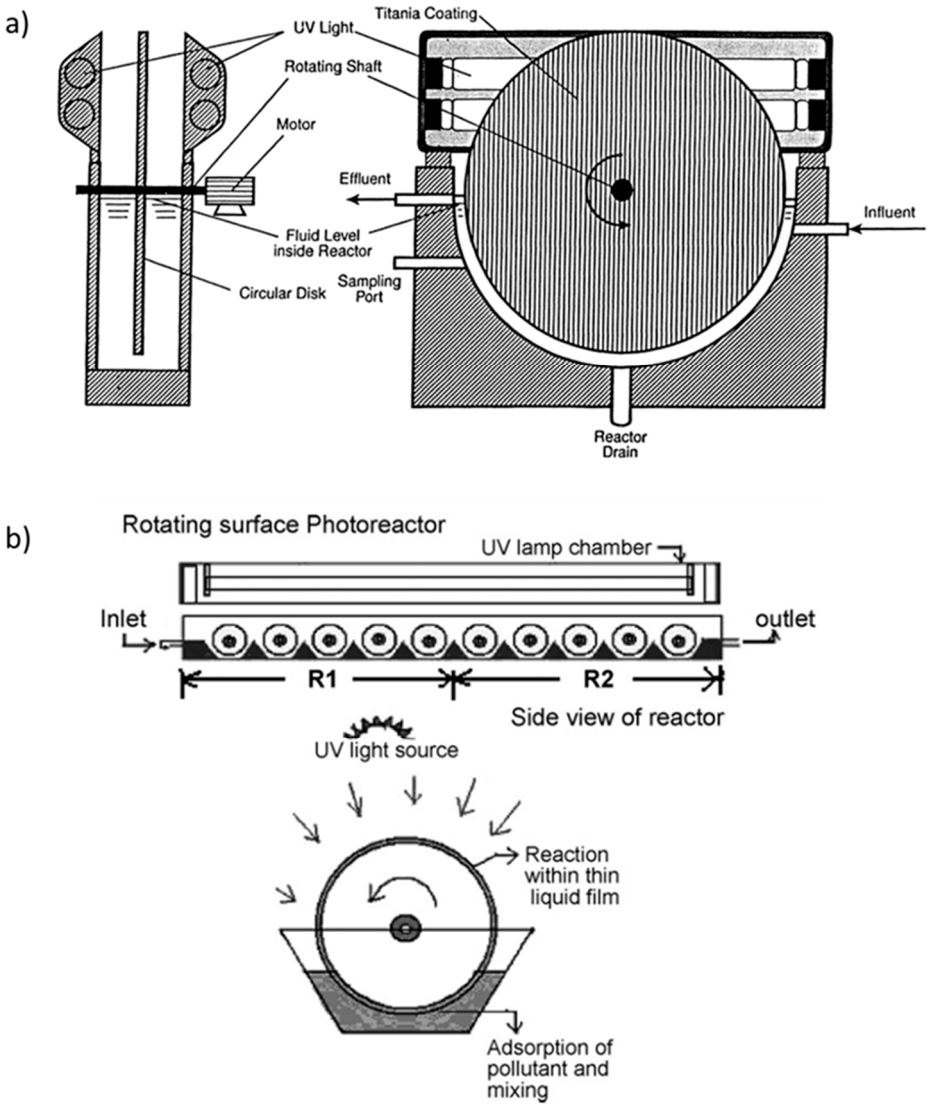


**Figure 7.** (**a**) Schematic illustration of a rotating disk photocatalytic reactor [53], and (**b**) a rotating tube photocatalytic reactor [54].

## 5. Photocatalytic Materials Engineering

ZnO and $TiO_2$ are the most commonly used metal oxide materials for photocatalysis. However, several factors limit the performances of the photocatalytic reaction. For example, the charge carrier recombination can limit the number of available electron-hole pairs for the reaction, which leads to the reduced efficiency of the degradation. Another limitation is related to the charge separation dependency on the energy of the incident light. To improve the performance of the photocatalyst, therefore, dopants or composite photocatalyst design has been employed. Here, we exemplify ZnO photocatalysts to demonstrate how the photocatalytic performance can be improved by modifying the pristine ZnO material. As mentioned previously, the efficiency of the photocatalyst is governed by the photo-induced electron-hole pairs. The photocatalysis process for the dye degradation can only proceed when the incident light has greater energy than the ZnO materials' bandgap. In this way, only UV light with a wavelength less than 387 nm can be utilized for the photocatalysis process. ZnO has three different crystal structures: hexagonal wurtzite, cubic zincblende

and rocksalt. The hexagonal wurtzite is the most thermodynamically stable structure under room temperature, where four $O^{2-}$ anions surround each $Zn^{2+}$ cation at the corners of a tetrahedron and vice versa [55]. Doping appropriate materials into the ZnO crystal can narrow the bandgap and inhibit the recombination of the photo-induced electrons and holes, leading to enhanced photocatalytic performance under the visible light region [56]. Doping with metal ions can narrow the ZnO bandgap, resulting in a shift of the absorption edge to the visible range. Many metal ion dopants have been studied, including copper, cadmium, tin, cobalt, aluminum, and iron [57–62]. Mohan et al. found that doping with copper can cause surface defects, which can serve as favorable trap sites of the electrons or holes to reduce their recombination and enhance the performance [63]. Ba-Abbad et al. incorporated iron ions ($Fe^{3+}$) into ZnO via the sol-gel technique [64]. The results indicated longer wavelength absorption in the visible light range and a redshift of the bandgap. Furthermore, Karunakaran et al. studied the performance of cadmium doped ZnO; they concluded that the doping would not change much of the bandgap structure but reducing the grain size of the ZnO structure would destroy the microstructure [65].

In doping with a non-metal atom, the oxygen atoms are substituted by non-metal atoms, which will shift the valence band energy of ZnO upward and narrow its bandgap energy. Carbon (C), nitrogen (N), and sulfur (S) are promising candidates among non-metal atoms [56,66]. Yu et al. incorporated N into the ZnO crystals to form the N 2p states in the bandgap, which improves the visible light absorption and enhancement of the photocatalytic activity [56]. The incorporated N atoms can exist in the ZnO lattice's interstitial sites; the doped N can improve the visible light absorption and photocatalytic activity [67]. C-doped ZnO also showed an enhanced visible light absorption up to 700 nm [68].

Coupling ZnO crystals with guest materials, such as Ag, $Bi_2O_3$, ZnS, $MoS_2$, and $TiO_2$ to form a composite material can also improve photocatalytic activity [69–72]. In the composite material, ZnO is directly contacted with guest materials. The coupled materials have two different energy levels. Upon irradiation, the photo-induced electrons can be transferred from ZnO to the guest materials, which inhibits the recombination of the electron-hole pairs [34]. Ag is a promising metal to couple with ZnO to form the composite photocatalyst and has been studied extensively. The coupled Ag-ZnO material mainly plays two roles. The first is to reduce the hole-electron recombination due to the Schottky barrier at the metal-semiconductor interface [73]. The Ag's other function is to enhance the visible light absorption of the composite system induced by Ag's surface plasmonic absorption [74]. Similar strategies have been applied to improve the performance of the other metal oxide semiconductors, such as $TiO_2$, by changing the material's bandgap and preventing recombination of the holes and electrons. For example, nitrogen is doped into $TiO_2$ crystals for visible light photocatalysis [75,76]. Metal atoms, such as silver [77], copper [78], aluminum [79], and iron [80] have also been studied to enhance the photocatalytic performance of $TiO_2$ material.

Several strategies have been used to immobilize the photocatalyst on the substrate surface. The simplest one is to directly deposit a thin film on the substrate, as illustrated by Figure 8a [45]. The thin films can adopt different structures, such as a thick film with porous structures or a nanostructured thin film. However, the thin film's active surface area is limited, which can hinder the performance of photocatalysis. Structures with a higher loading amount and higher active surface area have been fabricated to increase the contact between the solution and the photocatalyst. For example, in Figure 8b, the $TiO_2$ nanoparticles were coated on fiberglass to enlarge the reaction area and enhance the degradation efficiency [81]. Figure 8c shows that the $TiO_2$ nanoparticles were coated onto the $SiO_2$ beads with high mechanical stability and surface area [82]. The function of the $SiO_2$ is to provide a supporter surface to load the catalyst. On the other hand, a composite structure, such as a Pt-coated ZnO nanorods array, shown in Figure 8d, was constructed to enhance photocatalytic efficiency by effectively separating the photo-induced electron-hole pairs [24].

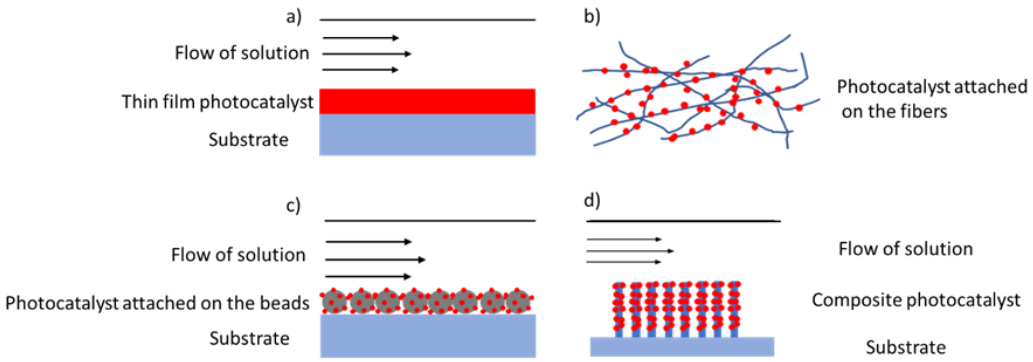


**Figure 8.** (**a**) Thin film photocatalyst, (**b**) photocatalyst attached on fibers, (**c**) photocatalyst attached on beads, and (**d**) composite photocatalyst.

Besides these traditional metal oxide photocatalysts, novel photocatalyst materials have been developed and introduced to reduce the contaminants in wastewater. Plasmonic photocatalysts have gained great attention owing to their enhanced efficiency under visible light. Different metal nanoparticles, such as gold [83], silver [84], and aluminum have been studied as the plasmonic photocatalyst and have shown great efficiency in the visible light region. A plasmonic photocatalyst contains the contact between a metal and a semiconductor, forming the Schottky junction that inhibits the electron-hole recombination [85]. One feature of the plasmonic photocatalyst is the localized surface plasmon resonance (LSPR) effect of the nanostructured noble metal, which is a strong oscillation of the free electrons stimulated by the incident light, resulting in enhanced light absorption and scattering [86].

Other novel photocatalytic materials, such as $BiSbO_4$ [87], $Nd_2Sn_2O_7$ [88,89], $(BiO)_2CO_3$ [90–94], $La_2Ti_2O_7$ [95], $PrVO_4$ [96], and $ZnTiO_3$ [97] have also been studied for degradation of the water contaminant.

In addition, some earth abundant, non-metal photocatalysts have been reported. For example, red phosphorus was prepared by a mechanical ball milling method and showed the enhanced photocatalytic performance under visible light [98]. Graphite-like carbon nitride (g-$C_3N_4$) is another metal-free, n-type semiconductor that can be used in photocatalysis due to its promising properties, such as unique electric, optical, structural and physiochemical properties [99–101].

## 6. Examples

The larger surface area of the microchannel is typically pursued to enhance the photocatalytic activities. In this regard, attempts have been made to increase the surface area of the microchannel. Lindstrom et al. designed a microfluidic reactor encompassing 11 parallel microchannels with 32 side lobes per channel, leading to a significant increase in the surface area (Figure 9) [48]. With such a high surface area, the authors enabled an extremely high loading factor of 66 g anatase $TiO_2$ per liter of methylene blue solution. Azzouz et al. increased the surface area of the microfluidic reactor by fabricating a multi-hierarchical micro-nano structure [47]. In particular, ZnO nanowires were subsequently grown on the micro-nano structure fabricated by deep reactive ion etching of silicon (Figure 10). Contaminated water containing benzene, toluene, ethylbenzene, m- p-xylenes, and o-xylene flowed through the microreactor for purification. The photocatalytic results demonstrated high photocatalytic efficiency, with degradation of the contaminated water up to 95% within 5s.

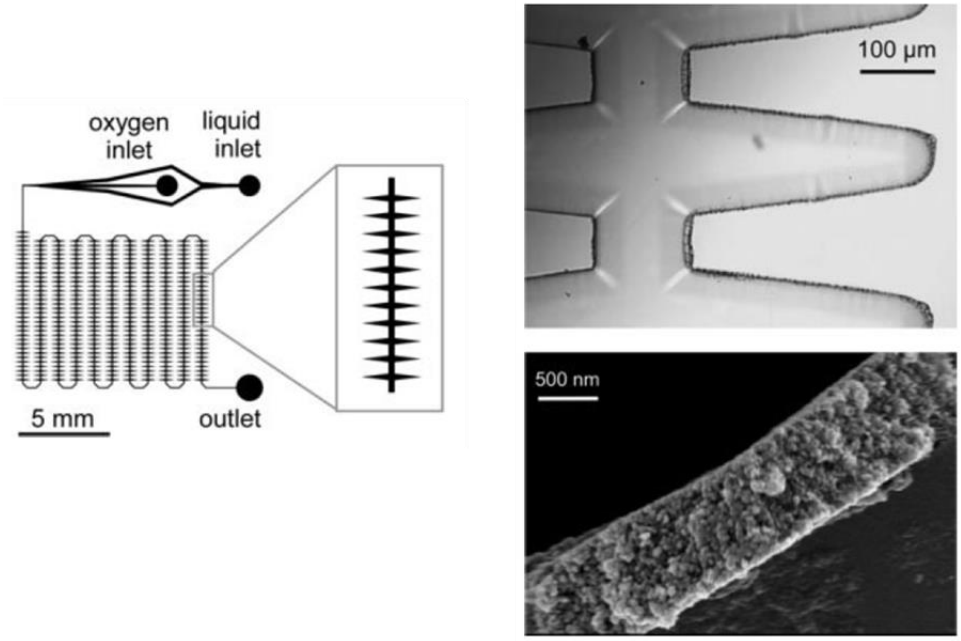


**Figure 9.** Channel with side lobes and the $TiO_2$ loaded on the channel wall [48].

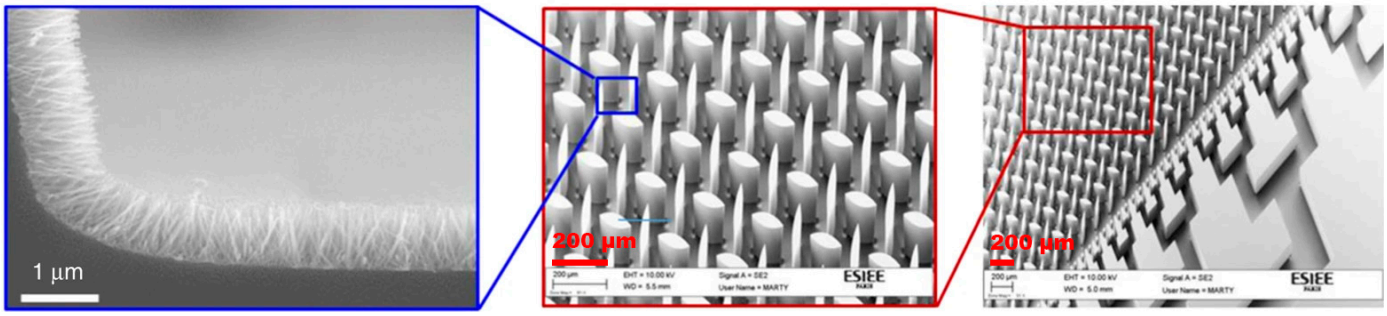


**Figure 10.** Hierarchical micro-nano structure (microstructure obtained by deep reactive ion, followed by growth of ZnO nanowires for the nanostructure) [47].

In addition to the design concept of adjusting channel shapes and surface area, a novel photocatalytic reactor, called a rotating disk photocatalytic reactor (RDPR), was reported [53]. In this type of reactor, a thin film of liquid containing the target compound is carried into the catalyst surface by a semicircular part of a rotating disk coated with $TiO_2$, as shown in Figure 7a. The photocatalytic reaction to remove the chlorinated phenols and pesticides occurs in the thin-film liquid under UV irradiation before the thin film rotates back to the vessel. A similar design concept was employed to achieve scale-up of the photocatalytic system. The multiple rotating tubes are equipped to carry the numerous liquid films simultaneously (Figure 7b) for the degradation of azo dye [54]. Like the single RDPR reactor, the thin film of liquid formed on the tube surface is exposed to UV radiation for the photocatalytic reaction.

Aran et al. demonstrated a new membrane microreactor concept for multiphase photocatalytic reactions (Figure 11) [102]. In this concept, the microfluidic channel was fabricated on a porous $\alpha$-$Al_2O_3$ substrate, and the $TiO_2$ photocatalyst was immobilized on the channel walls. The porous $\alpha$-$Al_2O_3$ allows the supply of the gas to the channel, and its hydrophobic property can prevent the water from leaking, enabling a stable gas-liquid-solid system. The result has shown that the membrane-assisted supply of $O_2$ enhanced the photocatalytic degradation of phenol and methylene blue.

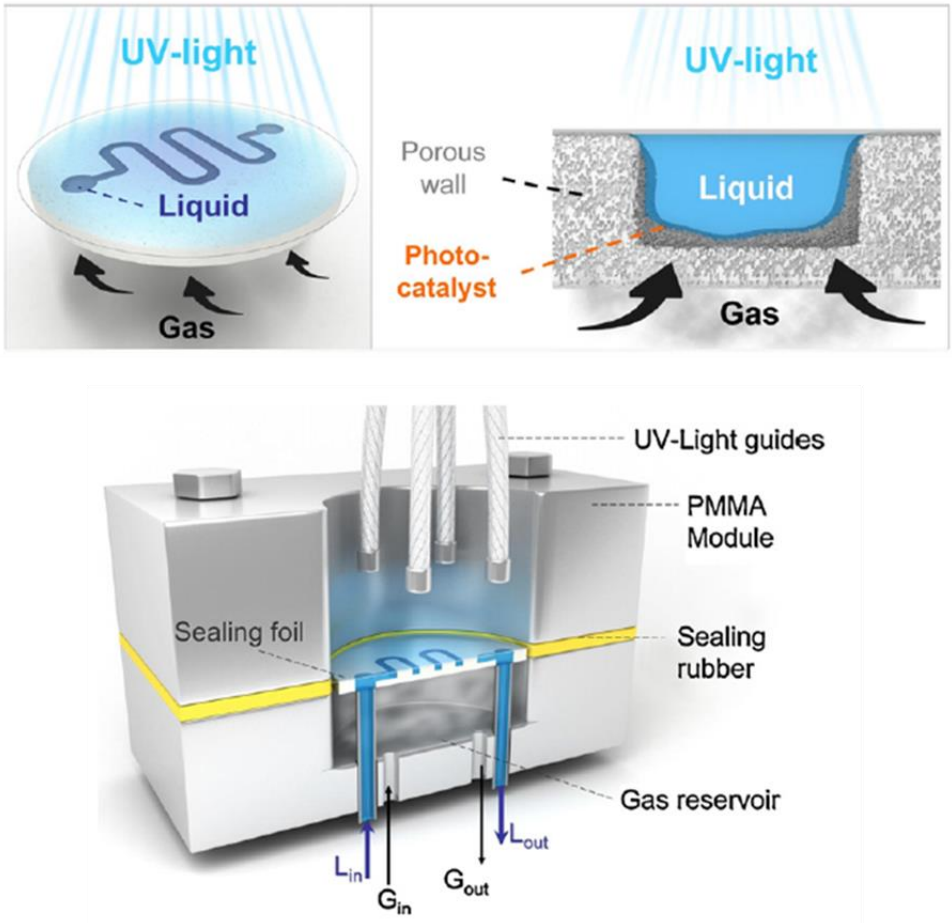


**Figure 11.** Schematic illustration of the photocatalytic reactor with the gas-liquid-solid system [102].

## 7. Summary and Future Perspective

In this review, different research aspects of microfluidic-based photocatalysis have been presented, including studying the reaction kinetics, design of the microreactor to enhance the performance, and the engineering of the catalyst efficiency. The previous studies have already proven that the photocatalytic microfluidic reactor has excellent potential to remove organic contaminants in water by taking advantage of its high efficiency, catalyst reusability, and continuous operation. Despite these advantages, many areas require further investigation before its real-world application.

- The majority of the reported photocatalytic microfluidic reactors use UV light sources. Typical UV lights have low energy efficiency. It will improve sustainability if one can replace the UV lights with sunlight. More studies in this area are needed.
- Not many studies are devoted to optimizing the utilization efficiency of photons at the reactor level. More studies in optimum photocatalytic reactor design that consider both optics and catalytic reactions are needed.
- The majority of the reported photocatalytic microfluidic reactors remain lab-scale and are not suited for large-scale deployment. More studies on scalable photocatalytic microreactors, including microstructured reactor design, are needed.
- Fundamental research to enlighten the photocatalytic reaction kinetics using scalable microfluidic devices in the labs is another area that will support the development of more efficient photocatalytic microreactors.

**Author Contributions:** Conceptualization: C.-H.C. (Chih-Hung Chang); writing original draft: Z.G., C.P.; review and editing: C.-H.C. (Chang-Ho Choi), C.-H.C. (Chih-Hung Chang). All authors have read and agreed to the published version of the manuscript.

**Funding:** This work was supported by the National Science Foundation, USA, grants CBET-1449383 NNCI-2025489, National Research Foundation of Korea (NRF) (No. 2019R1I1A3A01058865) and Walmart Manufacturing Innovation Foundation (29955421).

**Institutional Review Board Statement:** Not applicable.

**Informed Consent Statement:** Not applicable.

**Data Availability Statement:** Not applicable.

**Conflicts of Interest:** The authors declare no conflict of interest.

## References

1. Shanker, U.; Rani, M.; Jassal, V. Degradation of hazardous organic dyes in water by nanomaterials. *Environ. Chem. Lett.* **2017**, *15*, 623–642. [CrossRef]
2. Byrne, H.E.; Mazyck, D.W. Removal of trace level aqueous mercury by adsorption and photocatalysis on silica–titania composites. *J. Hazard. Mater.* **2009**, *170*, 915–919. [CrossRef]
3. Lu, Y.; Yuan, J.; Du, D.; Sun, B.; Yi, X. Monitoring long-term ecological impacts from release of Fukushima radiation water into ocean. *Geogr. Environ. Sustain.* **2021**, *2*, 95–98. [CrossRef]
4. Pandey, P.K.; Kass, P.H.; Soupir, M.L.; Biswas, S.; Singh, V.P. Contamination of water resources by pathogenic bacteria. *AMB Express* **2014**, *4*, 51. [CrossRef]
5. Lee, B.; Song, W.; Manna, B.; Yang, H.; Kim, J.; Kim, Y. Removal of color from wastewater using various ozonation techniques. In Proceedings of the 2007 International Forum on Strategic Technology, Ulaanbaatar, Mongolia, 3–6 October 2007; pp. 120–124.
6. Gouvêa, C.A.K.; Wypych, F.; Moraes, S.G.; Durán, N.; Nagata, N.; Peralta-Zamora, P. Semiconductor-assisted photocatalytic degradation of reactive dyes in aqueous solution. *Chemosphere* **2000**, *40*, 433–440. [CrossRef]
7. Sreethawong, T.; Ngamsinlapasathian, S.; Yoshikawa, S. Surfactant-aided sol–gel synthesis of mesoporous-assembled $TiO_2$–NiO mixed oxide nanocrystals and their photocatalytic azo dye degradation activity. *Chem. Eng. J.* **2012**, *192*, 292–300. [CrossRef]
8. Pare, B.; Jonnalagadda, S.B.; Tomar, H.; Singh, P.; Bhagwat, V.W. ZnO assisted photocatalytic degradation of acridine orange in aqueous solution using visible irradiation. *Desalination* **2008**, *232*, 80–90. [CrossRef]
9. Murruni, L.; Leyva, G.; Litter, M.I. Photocatalytic removal of Pb(II) over $TiO_2$ and Pt-$TiO_2$ powders. *Catal. Today* **2007**, *129*, 127–135. [CrossRef]
10. Ku, Y.; Lin, C.-N.; Hou, W.-M. Characterization of coupled NiO/$TiO_2$ photocatalyst for the photocatalytic reduction of Cr(VI) in aqueous solution. *J. Mol. Catal. A Chem.* **2011**, *349*, 20–27. [CrossRef]
11. Elmolla, E.S.; Chaudhuri, M. Degradation of amoxicillin, ampicillin and cloxacillin antibiotics in aqueous solution by the UV/ZnO photocatalytic process. *J. Hazard. Mater.* **2010**, *173*, 445–449. [CrossRef]
12. Katsumata, H.; Sada, M.; Nakaoka, Y.; Kaneco, S.; Suzuki, T.; Ohta, K. Photocatalytic degradation of diuron in aqueous solution by platinized $TiO_2$. *J. Hazard. Mater.* **2009**, *171*, 1081–1087. [CrossRef]
13. Shi, W.; Ren, H.; Li, M.; Shu, K.; Xu, Y.; Yan, C.; Tang, Y. Tetracycline removal from aqueous solution by visible-light-driven photocatalytic degradation with low cost red mud wastes. *Chem. Eng. J.* **2020**, *382*, 122876. [CrossRef]
14. Liu, S.; Wang, N.; Zhang, Y.; Li, Y.; Han, Z.; Na, P. Efficient removal of radioactive iodide ions from water by three-dimensional $Ag_2O$-Ag/$TiO_2$ composites under visible light irradiation. *J. Hazard. Mater.* **2015**, *284*, 171–181. [CrossRef]
15. Li, Z.-J.; Huang, Z.-W.; Guo, W.-L.; Wang, L.; Zheng, L.-R.; Chai, Z.-F.; Shi, W.-Q. Enhanced photocatalytic removal of uranium(VI) from aqueous solution by magnetic $TiO_2$/$Fe_3O_4$ and its graphene composite. *Environ. Sci. Technol.* **2017**, *51*, 5666–5674. [CrossRef]
16. Liang, P.-L.; Yuan, L.-Y.; Deng, H.; Wang, X.-C.; Wang, L.; Li, Z.-J.; Luo, S.-Z.; Shi, W.-Q. Photocatalytic reduction of uranium(VI) by magnetic $ZnFe_2O_4$ under visible light. *Appl. Catal. B* **2020**, *267*, 118688. [CrossRef]
17. Bonetta, S.; Bonetta, S.; Motta, F.; Strini, A.; Carraro, E. Photocatalytic bacterial inactivation by $TiO_2$-coated surfaces. *AMB Express* **2013**, *3*, 59. [CrossRef] [PubMed]
18. Qin, F.; Zhao, H.; Li, G.; Yang, H.; Li, J.; Wang, R.; Liu, Y.; Hu, J.; Sun, H.; Chen, R. Size-tunable fabrication of multifunctional $Bi_2O_3$ porous nanospheres for photocatalysis, bacteria inactivation and template-synthesis. *Nanoscale* **2014**, *6*, 5402. [CrossRef]
19. Jiang, Y.; Sun, Y.; Liu, H.; Zhu, F.; Yin, H. Solar photocatalytic decolorization of C.I. Basic Blue 41 in an aqueous suspension of $TiO_2$–ZnO. *Dyes Pigm.* **2008**, *78*, 77–83. [CrossRef]
20. Wang, L.; Zheng, Y.; Li, X.; Dong, W.; Tang, W.; Chen, B.; Li, C.; Li, X.; Zhang, T.; Xu, W. Nanostructured porous ZnO film with enhanced photocatalytic activity. *Thin Solid Films* **2011**, *519*, 5673–5678. [CrossRef]
21. Kim, K.-J.; Kreider, P.B.; Choi, C.; Chang, C.-H.; Ahn, H.-G. Visible-light-sensitive Na-doped p-type flower-like ZnO photocatalysts synthesized via a continuous flow microreactor. *RSC Adv.* **2013**, *3*, 12702–12710. [CrossRef]
22. Raza, W.; Faisal, S.M.; Owais, M.; Bahnemann, D.; Muneer, M. Facile fabrication of highly efficient modified ZnO photocatalyst with enhanced photocatalytic, antibacterial and anticancer activity. *RSC Adv.* **2016**, *6*, 78335–78350. [CrossRef]

23. He, Z.; Li, Y.; Zhang, Q.; Wang, H. Capillary microchannel-based microreactors with highly durable ZnO/$TiO_2$ nanorod arrays for rapid, high efficiency and continuous-flow photocatalysis. *Appl. Catal. B* **2010**, *93*, 376–382. [CrossRef]
24. Zhang, Q.; Zhang, Q.; Wang, H.; Li, Y. A high efficiency microreactor with Pt/ZnO nanorod arrays on the inner wall for photodegradation of phenol. *J. Hazard. Mater.* **2013**, *254–255*, 318–324. [CrossRef] [PubMed]
25. Chakrabarti, S.; Dutta, B.K. Photocatalytic degradation of model textile dyes in wastewater using ZnO as semiconductor catalyst. *J. Hazard. Mater.* **2004**, *112*, 269–278. [CrossRef] [PubMed]
26. Fenton, H.J.H. LXXIII. Oxidation of tartaric acid in presence of iron. *J. Chem. Soc. Trans.* **1894**, *65*, 899–910. [CrossRef]
27. Pignatello, J.J.; Oliveros, E.; MacKay, A. Advanced Oxidation Processes for Organic Contaminant Destruction Based on the Fenton Reaction and Related Chemistry. *Crit. Rev. Environ. Sci. Technol.* **2006**, *36*, 1–84. [CrossRef]
28. Ye, J.; Yu, J.; Zhang, Y.; Chen, M.; Liu, X.; Zhou, S.; He, Z. Light-driven carbon dioxide reduction to methane by Methanosarcina barkeri-CdS biohybrid. *Appl. Catal. B* **2019**, *257*, 117916. [CrossRef]
29. Yin, K.; Wang, Q.; Lv, M.; Chen, L. Microorganism remediation strategies towards heavy metals. *Chem. Eng. J.* **2019**, *360*, 1553–1563. [CrossRef]
30. Zuo, W.; Yu, Y.; Huang, H. Making waves: Microbe-photocatalyst hybrids may provide new opportunities for treating heavy metal polluted wastewater. *Water Res.* **2021**, *195*, 116984. [CrossRef]
31. Zhang, X.; Wang, Y.; Hou, F.; Li, H.; Yang, Y.; Zhang, X.; Yang, Y.; Wang, Y. Effects of Ag loading on structural and photocatalytic properties of flower-like ZnO microspheres. *Appl. Surf. Sci.* **2017**, *391*, 476–483. [CrossRef]
32. Carbonaro, S.; Sugihara, M.N.; Strathmann, T.J. Continuous-flow photocatalytic treatment of pharmaceutical micropollutants: Activity, inhibition, and deactivation of $TiO_2$ photocatalysts in wastewater effluent. *Appl. Catal. B* **2013**, *129*, 1–12. [CrossRef]
33. Wang, N.; Zhang, X.; Wang, Y.; Yu, W.; Chan, H.L.W. Microfluidic reactors for photocatalytic water purification. *Lab Chip* **2014**, *14*, 1074–1082. [CrossRef]
34. Lee, K.M.; Lai, C.W.; Ngai, K.S.; Juan, J.C. Recent developments of zinc oxide based photocatalyst in water treatment technology: A review. *Water Res.* **2016**, *88*, 428–448. [CrossRef] [PubMed]
35. Daneshvar, N.; Salari, D.; Khataee, A.R. Photocatalytic degradation of azo dye acid red 14 in water on ZnO as an alternative catalyst to $TiO_2$. *J. Photochem. Photobiol. A* **2004**, *162*, 317–322. [CrossRef]
36. Samadi, M.; Zirak, M.; Naseri, A.; Khorashadizade, E.; Moshfegh, A.Z. Recent progress on doped ZnO nanostructures for visible-light photocatalysis. *Thin Solid Films* **2016**, *605*, 2–19. [CrossRef]
37. Behnajady, M.A.; Modirshahla, N.; Daneshvar, N.; Rabbani, M. Photocatalytic degradation of an azo dye in a tubular continuous-flow photoreactor with immobilized $TiO_2$ on glass plates. *Chem. Eng. J.* **2007**, *127*, 167–176. [CrossRef]
38. Meng, Z.; Zhang, X.; Qin, J. A high efficiency microfluidic-based photocatalytic microreactor using electrospun nanofibrous $TiO_2$ as a photocatalyst. *Nanoscale* **2013**, *5*, 4687–4690. [CrossRef]
39. Roselin, L.S.; Rajarajeswari, G.R.; Selvin, R.; Sadasivam, V.; Sivasankar, B.; Rengaraj, K. Sunlight/ZnO-mediated photocatalytic degradation of Reactive Red 22 using thin film flat bed flow photoreactor. *Solar Energy* **2002**, *73*, 281–285. [CrossRef]
40. Moussavi, G.; Jiani, F.; Shekoohiyan, S. Advanced reduction of Cr(VI) in real chrome-plating wastewater using a VUV photoreactor: Batch and continuous-flow experiments. *Sep. Purif. Technol.* **2015**, *151*, 218–224. [CrossRef]
41. Corbel, S.; Becheikh, N.; Roques-Carmes, T.; Zahraa, O. Mass transfer measurements and modeling in a microchannel photocatalytic reactor. *Chem. Eng. Res. Des.* **2014**, *92*, 657–662. [CrossRef]
42. Mendoza, C.; Emmanuel, N.; Páez, C.A.; Dreesen, L.; Monbaliu, J.C.M.; Heinrichs, B. Transitioning from conventional batch to microfluidic processes for the efficient singlet oxygen photooxygenation of methionine. *J. Photochem. Photobiol. A* **2018**, *356*, 193–200. [CrossRef]
43. Zhan, X.; Yan, C.; Zhang, Y.; Rinke, G.; Rabsch, G.; Klumpp, M.; Schäfer, A.I.; Dittmeyer, R. Investigation of the reaction kinetics of photocatalytic pollutant degradation under defined conditions with inkjet-printed $TiO_2$ films—from batch to a novel continuous-flow microreactor. *React. Chem. Eng.* **2020**, *5*, 1658–1670. [CrossRef]
44. Matsushita, Y.; Ohba, N.; Kumada, S.; Sakeda, K.; Suzuki, T.; Ichimura, T. Photocatalytic reactions in microreactors. *Chem. Eng. J.* **2008**, *135*, S303–S308. [CrossRef]
45. Visan, A.; Rafieian, D.; Ogieglo, W.; Lammertink, R.G.H. Modeling intrinsic kinetics in immobilized photocatalytic microreactors. *Appl. Catal. B* **2014**, *150–151*, 93–100. [CrossRef]
46. Castedo, A.; Mendoza, E.; Angurell, I.; Llorca, J. Silicone microreactors for the photocatalytic generation of hydrogen. *Catal. Today* **2016**, *273*, 106–111. [CrossRef]
47. Azzouz, I.; Habba, Y.G.; Capochichi-Gnambodoe, M.; Marty, F.; Vial, J.; Leprince-Wang, Y.; Bourouina, T. Zinc oxide nano-enabled microfluidic reactor for water purification and its applicability to volatile organic compounds. *Microsyst. Nanoeng.* **2018**, *4*, 17093. [CrossRef]
48. Lindstrom, H.; Wootton, R.; Iles, A. High surface area titania photocatalytic microfluidic reactors. *AIChE J.* **2007**, *53*, 695–702. [CrossRef]
49. Han, Z.; Li, J.; He, W.; Li, S.; Li, Z.; Chu, J.; Chen, Y. A microfluidic device with integrated ZnO nanowires for photodegradation studies of methylene blue under different conditions. *Microelectron. Eng.* **2013**, *111*, 199–203. [CrossRef]
50. Wang, N.; Liu, Z.; Chan, N.Y.; Chan, H.L.W.; Zhang, X. Photocatalytic Microfluidic Reactor with a Novel Compound Catalyst Film Using Solar Energy. In Proceedings of the Sixteenth International Conference on Miniaturized Systems for Chemistry and Life Sciences (μTAS 2012), Okinawa, Japan, 28 October 2012; pp. 1993–1995.

51. Wang, N.; Zhang, X.; Chen, B.; Song, W.; Chan, N.Y.; Chan, H.L.W. Microfluidic photoelectrocatalytic reactors for water purification with an integrated visible-light source. *Lab Chip* **2012**, *12*, 3983–3990. [CrossRef]
52. Kim, H.-i.; Kim, D.; Kim, W.; Ha, Y.-C.; Sim, S.-J.; Kim, S.; Choi, W. Anodic $TiO_2$ nanotube layer directly formed on the inner surface of Ti pipe for a tubular photocatalytic reactor. *Appl. Catal. A* **2016**, *521*, 174–181. [CrossRef]
53. Dionysiou, D.D.; Khodadoust, A.P.; Kern, A.M.; Suidan, M.T.; Baudin, I.; Laîné, J.-M. Continuous-mode photocatalytic degradation of chlorinated phenols and pesticides in water using a bench-scale $TiO_2$ rotating disk reactor. *Appl. Catal. B* **2000**, *24*, 139–155. [CrossRef]
54. Damodar, R.A.; Swaminathan, T. Performance evaluation of a continuous flow immobilized rotating tube photocatalytic reactor (IRTPR) immobilized with $TiO_2$ catalyst for azo dye degradation. *Chem. Eng. J.* **2008**, *144*, 59–66. [CrossRef]
55. Özgür, Ü.; Alivov, Y.I.; Liu, C.; Teke, A.; Reshchikov, M.A.; Doğan, S.; Avrutin, V.; Cho, S.-J.; Morkoç, H. A comprehensive review of ZnO materials and devices. *J. Appl. Phys.* **2005**, *98*, 041301. [CrossRef]
56. Yu, W.; Zhang, J.; Peng, T. New insight into the enhanced photocatalytic activity of N-, C- and S-doped ZnO photocatalysts. *Appl. Catal. B* **2016**, *181*, 220–227. [CrossRef]
57. Zhang, D.; Zeng, F. Visible light-activated cadmium-doped ZnO nanostructured photocatalyst for the treatment of methylene blue dye. *J. Mater. Sci.* **2012**, *47*, 2155–2161. [CrossRef]
58. Wu, C.; Shen, L.; Yu, H.; Zhang, Y.-C.; Huang, Q. Solvothermal synthesis of Cu-doped ZnO nanowires with visible light-driven photocatalytic activity. *Mater. Lett.* **2012**, *74*, 236–238. [CrossRef]
59. Sun, J.-H.; Dong, S.-Y.; Feng, J.-L.; Yin, X.-J.; Zhao, X.-C. Enhanced sunlight photocatalytic performance of Sn-doped ZnO for Methylene Blue degradation. *J. Mol. Catal. A Chem.* **2011**, *335*, 145–150. [CrossRef]
60. Wang, C.; Zhao, J.; Wang, X.; Mai, B.; Sheng, G.; Peng, P.a.; Fu, J. Preparation, characterization and photocatalytic activity of nano-sized ZnO/$SnO_2$ coupled photocatalysts. *Appl. Catal. B* **2002**, *39*, 269–279. [CrossRef]
61. Ahmad, M.; Ahmed, E.; Zhang, Y.; Khalid, N.R.; Xu, J.; Ullah, M.; Hong, Z. Preparation of highly efficient Al-doped ZnO photocatalyst by combustion synthesis. *Curr. Appl. Phys.* **2013**, *13*, 697–704. [CrossRef]
62. Saleh, R.; Djaja, N.F. UV light photocatalytic degradation of organic dyes with Fe-doped ZnO nanoparticles. *Superlattices Microstruct.* **2014**, *74*, 217–233. [CrossRef]
63. Mohan, R.; Krishnamoorthy, K.; Kim, S.-J. Enhanced photocatalytic activity of Cu-doped ZnO nanorods. *Solid State Commun.* **2012**, *152*, 375–380. [CrossRef]
64. Ba-Abbad, M.M.; Kadhum, A.A.H.; Mohamad, A.B.; Takriff, M.S.; Sopian, K. Visible light photocatalytic activity of $Fe^{3+}$-doped ZnO nanoparticle prepared via sol–gel technique. *Chemosphere* **2013**, *91*, 1604–1611. [CrossRef]
65. Karunakaran, C.; Vijayabalan, A.; Manikandan, G. Photocatalytic and bactericidal activities of hydrothermally synthesized nanocrystalline Cd-doped ZnO. *Superlattices Microstruct.* **2012**, *51*, 443–453. [CrossRef]
66. Chen, L.-C.; Tu, Y.-J.; Wang, Y.-S.; Kan, R.-S.; Huang, C.-M. Characterization and photoreactivity of N-, S-, and C-doped ZnO under UV and visible light illumination. *J. Photochem. Photobiol. A* **2008**, *199*, 170–178. [CrossRef]
67. Sudrajat, H.; Hartuti, S. Easily separable N-doped ZnO microspheres with high photocatalytic activity under visible light. *Mater. Res. Bull.* **2018**, *102*, 319–323. [CrossRef]
68. Zhou, X.; Li, Y.; Peng, T.; Xie, W.; Zhao, X. Synthesis, characterization and its visible-light-induced photocatalytic property of carbon doped ZnO. *Mater. Lett.* **2009**, *63*, 1747–1749. [CrossRef]
69. Balachandran, S.; Swaminathan, M. Facile Fabrication of Heterostructured $Bi_2O_3$–ZnO Photocatalyst and Its Enhanced Photocatalytic Activity. *J. Phys. Chem. C* **2012**, *116*, 26306–26312. [CrossRef]
70. Vaiano, V.; Matarangolo, M.; Murcia, J.J.; Rojas, H.; Navío, J.A.; Hidalgo, M.C. Enhanced photocatalytic removal of phenol from aqueous solutions using ZnO modified with Ag. *Appl. Catal. B* **2018**, *225*, 197–206. [CrossRef]
71. Hong, E.; Kim, J.H. Oxide content optimized ZnS–ZnO heterostructures via facile thermal treatment process for enhanced photocatalytic hydrogen production. *Int. J. Hydrog. Energy* **2014**, *39*, 9985–9993. [CrossRef]
72. Yuan, Y.-J.; Wang, F.; Hu, B.; Lu, H.-W.; Yu, Z.-T.; Zou, Z.-G. Significant enhancement in photocatalytic hydrogen evolution from water using a $MoS_2$ nanosheet-coated ZnO heterostructure photocatalyst. *Dalton Trans.* **2015**, *44*, 10997–11003. [CrossRef]
73. Ren, C.; Yang, B.; Wu, M.; Xu, J.; Fu, Z.; Lv, Y.; Guo, T.; Zhao, Y.; Zhu, C. Synthesis of Ag/ZnO nanorods array with enhanced photocatalytic performance. *J. Hazard. Mater.* **2010**, *182*, 123–129. [CrossRef]
74. Liu, H.; Hu, Y.; Zhang, Z.; Liu, X.; Jia, H.; Xu, B. Synthesis of spherical Ag/ZnO heterostructural composites with excellent photocatalytic activity under visible light and UV irradiation. *Appl. Surf. Sci.* **2015**, *355*, 644–652. [CrossRef]
75. Varley, J.B.; Janotti, A.; Van de Walle, C.G. Mechanism of Visible-Light Photocatalysis in Nitrogen-Doped $TiO_2$. *Adv. Mater.* **2011**, *23*, 2343–2347. [CrossRef]
76. Mrowetz, M.; Balcerski, W.; Colussi, A.J.; Hoffmann, M.R. Oxidative Power of Nitrogen-Doped $TiO_2$ Photocatalysts under Visible Illumination. *J. Phys. Chem. B* **2004**, *108*, 17269–17273. [CrossRef]
77. Cao, Y.; Tan, H.; Shi, T.; Tang, T.; Li, J. Preparation of Ag-doped $TiO_2$ nanoparticles for photocatalytic degradation of acetamiprid in water. *J. Chem. Technol. Biotechnol.* **2008**, *83*, 546–552. [CrossRef]
78. Colón, G.; Maicu, M.; Hidalgo, M.C.; Navío, J.A. Cu-doped $TiO_2$ systems with improved photocatalytic activity. *Appl. Catal. B* **2006**, *67*, 41–51. [CrossRef]
79. Murashkina, A.A.; Murzin, P.D.; Rudakova, A.V.; Ryabchuk, V.K.; Emeline, A.V.; Bahnemann, D.W. Influence of the Dopant Concentration on the Photocatalytic Activity: Al-Doped $TiO_2$. *J. Phys. Chem. C* **2015**, *119*, 24695–24703. [CrossRef]

80. Wang, C.-Y.; Bahnemann, D.W.; Dohrmann, J.K. A novel preparation of iron-doped $TiO_2$ nanoparticles with enhanced photocatalytic activity. *Chem. Commun.* **2000**, 1539–1540. [CrossRef]
81. Li, L.; Chen, R.; Zhu, X.; Wang, H.; Wang, Y.; Liao, Q.; Wang, D. Optofluidic Microreactors with $TiO_2$-Coated Fiberglass. *ACS Appl. Mater. Interfaces* **2013**, *5*, 12548–12553. [CrossRef]
82. Yoon, T.-H.; Hong, L.-Y.; Kim, D.-P. Photocatalytic reaction using novel inorganic polymer derived packed bed microreactor with modified $TiO_2$ microbeads. *Chem. Eng. J.* **2011**, *167*, 666–670. [CrossRef]
83. Wen, Y.; Liu, B.; Zeng, W.; Wang, Y. Plasmonic photocatalysis properties of Au nanoparticles precipitated anatase/rutile mixed $TiO_2$ nanotubes. *Nanoscale* **2013**, *5*, 9739–9746. [CrossRef] [PubMed]
84. Wang, P.; Huang, B.; Zhang, Q.; Zhang, X.; Qin, X.; Dai, Y.; Zhan, J.; Yu, J.; Liu, H.; Lou, Z. Highly Efficient Visible Light Plasmonic Photocatalyst Ag@Ag(Br, I). *Chem. Eur. J.* **2010**, *16*, 10042–10047. [CrossRef] [PubMed]
85. Zhang, X.; Chen, Y.L.; Liu, R.-S.; Tsai, D.P. Plasmonic photocatalysis. *Rep. Prog. Phys.* **2013**, *76*, 046401. [CrossRef]
86. Wang, C.; Astruc, D. Nanogold plasmonic photocatalysis for organic synthesis and clean energy conversion. *Chem. Soc. Rev.* **2014**, *43*, 7188–7216. [CrossRef] [PubMed]
87. Lin, X.; Huang, F.; Wang, W.; Zhang, K. A novel photocatalyst $BiSbO_4$ for degradation of methylene blue. *Appl. Catal. A* **2006**, *307*, 257–262. [CrossRef]
88. Zinatloo-Ajabshir, S.; Morassaei, M.S.; Salavati-Niasari, M. Facile synthesis of $Nd_2Sn_2O_7$-$SnO_2$ nanostructures by novel and environment-friendly approach for the photodegradation and removal of organic pollutants in water. *J. Environ. Manag.* **2019**, *233*, 107–119. [CrossRef] [PubMed]
89. Zinatloo-Ajabshir, S.; Morassaei, M.S.; Salavati-Niasari, M. Eco-friendly synthesis of $Nd_2Sn_2O_7$–based nanostructure materials using grape juice as green fuel as photocatalyst for the degradation of erythrosine. *Compos. B. Eng.* **2019**, *167*, 643–653. [CrossRef]
90. Zheng, Y.; Duan, F.; Chen, M.; Xie, Y. Synthetic $Bi_2O_2CO_3$ nanostructures: Novel photocatalyst with controlled special surface exposed. *J. Mol. Catal. A Chem.* **2010**, *317*, 34–40. [CrossRef]
91. Madhusudan, P.; Ran, J.; Zhang, J.; Yu, J.; Liu, G. Novel urea assisted hydrothermal synthesis of hierarchical $BiVO_4/Bi_2O_2CO_3$ nanocomposites with enhanced visible-light photocatalytic activity. *Appl. Catal. B* **2011**, *110*, 286–295. [CrossRef]
92. Zhu, G.; Hojamberdiev, M.; Katsumata, K.-I.; Cai, X.; Matsushita, N.; Okada, K.; Liu, P.; Zhou, J. Heterostructured $Fe_3O_4/Bi_2O_2CO_3$ photocatalyst: Synthesis, characterization and application in recyclable photodegradation of organic dyes under visible light irradiation. *Mater. Chem. Phys.* **2013**, *142*, 95–105. [CrossRef]
93. Dong, F.; Li, Q.; Zhang, W.; Guan, M.; Ho, W.-K.; Wu, Z. Synthesis of flower-like, pinon-like and faceted nanoplates $(BiO)_2CO_3$ micro/nanostructures with morphology-dependent photocatalytic activity. *Mater. Chem. Phys.* **2013**, *142*, 381–386. [CrossRef]
94. Li, Q.; Liu, H.; Dong, F.; Fu, M. Hydrothermal formation of N-doped $(BiO)_2CO_3$ honeycomb-like microspheres photocatalysts with bismuth citrate and dicyandiamide as precursors. *J. Colloid Interface Sci.* **2013**, *408*, 33–42. [CrossRef]
95. Onozuka, K.; Kawakami, Y.; Imai, H.; Yokoi, T.; Tatsumi, T.; Kondo, J.N. Perovskite-type $La_2Ti_2O_7$ mesoporous photocatalyst. *J. Solid State Chem.* **2012**, *192*, 87–92. [CrossRef]
96. Monsef, R.; Ghiyasiyan-Arani, M.; Amiri, O.; Salavati-Niasari, M. Sonochemical synthesis, characterization and application of $PrVO_4$ nanostructures as an effective photocatalyst for discoloration of organic dye contaminants in wastewater. *Ultrason. Sonochem.* **2020**, *61*, 104822. [CrossRef]
97. Salavati-Niasari, M.; Soofivand, F.; Sobhani-Nasab, A.; Shakouri-Arani, M.; Yeganeh Faal, A.; Bagheri, S. Synthesis, characterization, and morphological control of $ZnTiO_3$ nanoparticles through sol-gel processes and its photocatalyst application. *Adv. Powder Technol.* **2016**, *27*, 2066–2075. [CrossRef]
98. Ansari, S.A.; Ansari, M.S.; Cho, M.H. Metal free earth abundant elemental red phosphorus: A new class of visible light photocatalyst and photoelectrode materials. *Phys. Chem. Chem. Phys.* **2016**, *18*, 3921–3928. [CrossRef] [PubMed]
99. Wen, J.; Xie, J.; Chen, X.; Li, X. A review on g-$C_3N_4$-based photocatalysts. *Appl. Surf. Sci.* **2017**, *391*, 72–123. [CrossRef]
100. Moreira, N.F.F.; Sampaio, M.J.; Ribeiro, A.R.; Silva, C.G.; Faria, J.L.; Silva, A.M.T. Metal-free g-$C_3N_4$ photocatalysis of organic micropollutants in urban wastewater under visible light. *Appl. Catal. B* **2019**, *248*, 184–192. [CrossRef]
101. Fu, J.; Yu, J.; Jiang, C.; Cheng, B. g-$C_3N_4$-Based Heterostructured Photocatalysts. *Adv. Energy Mater.* **2018**, *8*, 1701503. [CrossRef]
102. Aran, H.C.; Salamon, D.; Rijnaarts, T.; Mul, G.; Wessling, M.; Lammertink, R.G.H. Porous Photocatalytic Membrane Microreactor (P2M2): A new reactor concept for photochemistry. *J. Photochem. Photobiol. A* **2011**, *225*, 36–41. [CrossRef]